AIAA Journal
Vol. 47, No. 10, October 2009

Computational Study of Roughness-Induced Boundary-Layer Noise

Qin Yang* and Meng Wang†
University of Notre Dame, Notre Dame, Indiana 46556

DOI: 10.2514/1.42343

As a first step toward predicting rough-wall boundary-layer noise, the sound radiated from a single hemispherical roughness element and a pair of roughness elements in a turbulent boundary layer at $Re_\theta = 7500$ is investigated. The roughness height is 3.6% of the boundary-layer thickness, or 95 wall units. The flowfield is obtained from large-eddy simulation, and the results are validated against experimental measurements. Acoustic calculations are performed based on the Curle–Powell integral solution to the Lighthill equation for an acoustically compact hemisphere. The sound radiation is dominated by unsteady drag dipoles and their images in the wall. It is found that the spanwise dipole, which has been overlooked in previous studies of roughness noise, is of larger or similar strength compared with the streamwise dipole, and the viscous contribution to the drag dipoles is negligible in comparison with the pressure contribution. Important flow features contributing to sound radiation are identified by examining the unsteady surface-pressure field and the surrounding flow structures. Pressure fluctuations are strongest on the upstream part of the hemispheric surface near the base due to impingement of incoming turbulent eddies and their interaction with horseshoe vortices. On the back surface of the hemisphere, pressure fluctuations are relatively weak, indicating that shear-layer separation and vortex shedding do not produce significant self-noise from the hemisphere. In the case with two hemispheres, the wake of the upstream hemisphere is found to significantly enhance sound radiation from the downstream hemisphere, particularly in the streamwise direction and at high frequencies.

Nomenclature

c_0 = freestream sound speed
D = diameter of hemispherical roughness element
D_i = components of dipole source function
f = frequency
G = acoustic Green's function
h = roughness height
M = freestream Mach number
n_j = components of unit normal (into fluid) of surface S
p = pressure
p_a = acoustic pressure
p_{ij} = components of compressive stress tensor
R = distance between center of roughness element and observer
Re_θ = Reynolds number based on momentum thickness
Re_τ = Reynolds number based on friction velocity
r = distance between source and observer
r^* = distance between source and image observer
S = solid boundary of the source region
S_r = surface of the roughness element
T_{ij} = components of Lighthill stress tensor
t = observer time
U = mean streamwise velocity
U_∞ = freestream velocity
u, v, w = streamwise, wall-normal, and spanwise components of velocity
u_τ = friction velocity
V = mean wall-normal velocity or volume of source region
$\mathbf{x}$ = position vector for observer location
$\mathbf{x}^*$ = image of observer position in the wall
x, y, z = coordinates in streamwise, wall-normal, and spanwise directions
$\mathbf{y}$ = position vector for source region
$\mathbf{y}_c$ = central position of the base of roughness element
$\Delta x, \Delta y, \Delta z$ = grid spacing
δ = boundary-layer thickness
θ = momentum thickness
λ = acoustic wavelength
ν = kinematic viscosity
ρ = fluid density
τ = source time
τ_{ij} = components of viscous stress tensor
Φ_{pa} = sound pressure spectrum
ω = vorticity magnitude

Superscripts

(n) = quantity associated with nth roughness element
$'$ = fluctuation quantity
$+$ = quantity in wall units
$\bar{\ }$ = time-averaged quantity

I. Introduction

Turbulent boundary-layer flows over a smooth, rigid, and plane surface are known to be acoustically inefficient. The fluctuations in surface pressure, once thought of as acoustic dipoles, are in reality specular images of quadrupole sources arising from the fluctuating Reynolds stress in the boundary layer [1]. Although the fluctuating viscous shear stress on a wall is a valid dipole sound source [2–4], its magnitude is generally small in high-Reynolds-number boundary layers of practical interest.

The presence of roughness elements on a plane surface can, however, drastically enhance boundary-layer noise. One way for a rough surface to generate enhanced noise is diffraction. Roughness elements introduce a surface inhomogeneity, which facilitates the conversion of flow energy to acoustic energy. The diffraction

---

Presented as Paper 2905 at the 14th AIAA/CEAS Aeroacoustics Conference, Vancouver, Canada, 5–7 May 2008; received 28 November 2008; revision received 30 April 2009; accepted for publication 29 May 2009.

*Graduate Student, Department of Aerospace and Mechanical Engineering, 117 Hessert Laboratory. Student Member AIAA.

†Associate Professor, Department of Aerospace and Mechanical Engineering, 105 Hessert Laboratory. Member AIAA.

mechanism alters the acoustic source character from quadrupoles to dipoles [5,6] and thereby causes a significant increase in radiated noise levels, even if the flowfield (structure) is unchanged by surface roughness. In a series of theoretical investigations [5–7], Howe examined rough-wall noise produced by the diffraction mechanism. By using Lighthill's aeroacoustic theory [8] with an approximate hard-wall Green's function for acoustically compact roughness elements, the dipole nature of the roughness noise source was revealed explicitly. The sound intensity was found to vary as the sixth power of flow velocity. In Howe's theory, wall roughness is modeled by a distribution of hemispherical bosses. The dominant turbulent pressure sources (fluctuating Reynolds stress) are assumed to lie above the roughness elements and are not directly affected by the roughness elements. This effectively limits the height of roughness elements to within the buffer layer.

Another mechanism for roughness noise generation is the modification of near-wall turbulence. In the fully rough regime, with roughness heights in excess of the buffer-layer thickness, the flow around a roughness element behaves as a turbulent junction flow [9]. Noise can be generated by incoming turbulent eddies impinging on the roughness elements, unsteady vortical structures formed around the elements, and vortex shedding resulting from the separation and breakdown of shear layers around the elements. These nonlinear interactions between flow and roughness elements, which are difficult to quantify, provide a potentially stronger noise source mechanism than diffraction. Collectively, they exert unsteady drag forces on the roughness elements, which constitute acoustic dipole sources as described by Curle [10]. Theoretical models for noise were developed in terms of unsteady drag dipoles [11,12], and vortex shedding was generally regarded as the main source of drag fluctuations. To obtain the unsteady drag, empirical or semiempirical models were required. For instance, Glegg et al. [12] employed a semiempirical model for the bluff-body drag frequency spectrum to estimate the roughness dipole sound. They recently derived a relationship between the far-field acoustic spectrum and the wall-pressure wave-number–frequency spectrum, which was confirmed by experimental measurements [13,14].

Noise generated by flow over rough surfaces is of particular concern in naval applications because underwater vehicles inevitably develop rough surfaces due to continual exposure to seawater. The problem is severe also because underwater vehicles have relatively large surface-area-to-perimeter ratios, making rough-surface noise significant or even dominant compared with edge noise [13]. Such noise can not only affect the stealth operation of a submarine but also obscure the weak signals from a remote source that a passive sonar system aims to detect [15]. In aeronautical applications, roughness noise is a significant part of the airframe noise in a clean configuration, when high-lift devices such as flaps and slats are retracted. Based on experimental measurements and empirical correlations, Liu and Dowling [16] estimated that roughness noise may exceed trailing-edge noise at high frequencies for a Boeing-757-sized aircraft wing. Their analysis is based on diffraction theory, as in the analyses of Howe [5–7], and thus cannot be expected to accurately account for the nonlinear interaction of turbulent flow with roughness elements.

There have been only a few experimental investigations of roughness noise. Earlier experiments involved turbulent boundary layers [17,18] and pipe flows [19] and were focused on radiated noise, wall-pressure spectra, and their correlations with the mean velocity. Considerable discrepancies exist among the data even in terms of basic scaling laws, that is, the velocity scaling of the noise spectrum. A quantitative comparison of the experimental results is difficult because of disparate flow conditions and configurations. Overall, the source mechanisms and radiation characteristics of roughness noise are still not well understood, and there is a lack of predictive tools. This has prompted a number of recent theoretical, experimental, and numerical investigations (see [12–14,20–23]), including the present work. Experimental measurements and theoretical modeling are both limited in access to detailed turbulent source-field data, which can be provided by an accurate numerical simulation. In addition, physical insight into source mechanisms generated through a numerical study can be used to guide the development of predictive models for roughness noise.

The objectives of this study are to develop a computational methodology for rough-wall boundary-layer noise and, through an analysis of simulation data, better understand the noise generation mechanisms. The numerical approach is based on large-eddy simulation (LES) and Lighthill's aeroacoustic theory [8] with a half-space Green's function, which is valid for acoustically compact roughness elements. The dominant noise sources are represented in terms of net unsteady drag dipoles in the streamwise and spanwise directions and their images in the wall. The resulting sound field includes contributions from both diffraction of hydrodynamic pressure and roughness–turbulence interaction. Separation of the two effects is numerically difficult and physically not meaningful, because hydrodynamic pressure fluctuations are strongly coupled with the turbulence generation and modification induced by roughness elements. Instead, we study the source mechanisms by examining the acoustic dipole sources in relation to the surrounding flowfield, so that the flow regions and structures most important to sound generation can be identified.

To facilitate validation of flow simulation and gain clear physical insight into the noise generation processes, the simpler cases of turbulent boundary-layer flows over a single roughness element and a pair of elements are considered in the present study. The resulting flow and sound characteristics are analyzed, and source mechanisms are examined in relation to the surrounding flow dynamics. The acoustic results from the single-element flow are relevant to the noise of distributed roughness in the sparse limit. The case with two elements, aligned in the streamwise direction, allows an investigation of the effect of an upstream wake on sound generation. Although this does not fully account for the interactions existing in a general rough-wall boundary layer with distributed roughness, the qualitative conclusions drawn from this study regarding sound characters and source mechanisms are expected to be generally valid. Several important new findings have been obtained. The spanwise drag dipole, which has been overlooked in previous studies, is comparable to or stronger than the streamwise dipole. Vortex shedding and the unsteady wake, previously considered major sources of drag dipoles, are relatively unimportant. Rather, the drag dipoles are mainly produced by pressure fluctuations on the front part of the hemisphere as a result of incoming turbulent eddies interacting with horseshoe vortices. An upstream wake significantly enhances dipole radiation at intermediate to high frequencies because of elevated incoming turbulence intensity.

II. Computational Approach

For the low-Mach-number boundary-layer flows considered here, a hybrid method, which computes the turbulent source field separately from the radiated acoustic far field, provides the most efficient and accurate approach [24]. The turbulent boundary layers with a single roughness element and a pair of roughness elements are computed with LES. The far-field sound is calculated using Lighthill's aeroacoustic theory [8].

A. Flow-Simulation Method

To obtain acoustic source functions over a broad range of frequencies, LES is used to simulate the boundary-layer flows over a single roughness element and a pair of roughness elements. Simulations are carried out with a finite volume, unstructured-mesh LES code developed at Stanford University [25]. The cell-based numerical scheme is energy conservative and low dissipative, thus allowing accurate representation of a wide range of turbulence scales that are relevant to sound generation. The code is second-order accurate in both time and space. It employs a fully implicit, fractional-step time advancement and an algebraic multigrid Poisson solver for pressure. The effect of subgrid-scale motions is modeled using the dynamic Smagorinsky model.

To validate the numerical approach and understand sound generation mechanisms for an isolated roughness element, the boundary-layer flow over a single hemispherical roughness element, as in the experiment of Bennington [26] at the Virginia Polytechnic Institute and State University, is first considered. In the experiment, the boundary-layer thickness is $\delta = 39.3$ mm at a position 50.8 mm upstream of the hemisphere, the roughness height is $h = 1.4$ mm, and the freestream velocity is $U_\infty = 27.5$ m/s. Detailed velocity statistics were measured using three-velocity-component laser Doppler velocimetry (LDV) but no acoustic data are available. The computation is performed in a rectangular domain of size 5δ, 3δ, and 2δ in the streamwise (x), wall-normal (y), and spanwise (z) directions, respectively, as shown in Fig. 1. The hemisphere is based at the center of the plane wall, $x = y = z = 0$. The flow and geometric parameters are carefully selected to match the experiment. The momentum-thickness-based Reynolds number at the inlet is $Re_\theta = U_\infty\theta/\nu = 7500$, which corresponds to a friction Reynolds number of $Re_\tau = u_\tau\delta/\nu = 2666$. The roughness height is $h = D/2 = 0.036\delta$, where D is the diameter of the hemisphere. In terms of wall units, $h^+ = hu_\tau/\nu = 95$, which places the top of the hemisphere deep inside the logarithmic layer and makes the surface hydraulically rough.

The boundary conditions employed in the LES consist of a convective condition for the outlet, a stress-free condition for the top boundary, a no-slip condition for the bottom wall including the surface of the hemisphere, a periodic condition in the spanwise direction, and turbulent inflow at the inlet. The time-dependent turbulent inflow data are generated from a separate LES of a smooth-wall boundary layer using the "rescale and recycle" technique of Lund et al. [27].

Grid resolution is critically important in the vicinity of the hemisphere where incoming turbulent eddies are distorted and complex small-scale structures are generated. Examples of grid distributions near the hemisphere and inlet are shown in Fig. 2. The first off-wall grid spacing is approximately 2 wall units in the wall-normal direction. Away from the hemisphere, a typical LES boundary-layer resolution is adopted, with $\Delta x^+ \approx 50$, $\Delta z^+_{\min} \approx 25$, and $\Delta y^+_{\min} \approx 2$. The grid is smoothly coarsened in the wall-normal direction as the distance from the wall increases, and layers with different streamwise and spanwise resolutions are created to ensure the efficient use of grid cells. The total number of mesh cells is approximately 11.6×10^6 for the case of a single roughness element. The mesh for a pair of roughness elements is designed in a similar fashion, with a total of 12.1×10^6 mesh cells. The time step size in the simulations is determined based on a maximum Courant–Friedrichs–Lewy number of 1.5.

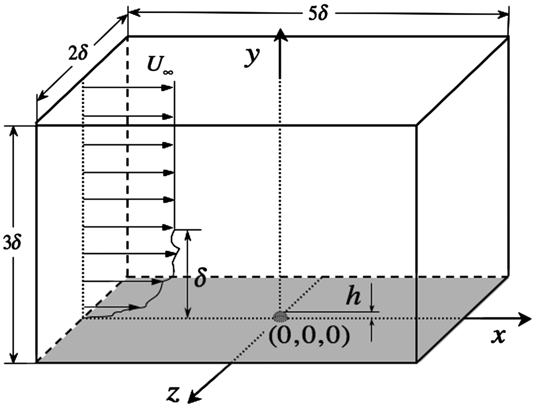

Fig. 1 Schematic of the computational domain for a single hemispherical roughness element on a plane wall.

B. Acoustic Formulation

In the presence of solid boundaries, a general integral solution to Lighthill's equation reads [15,28],

$$p_a(\mathbf{x}, t) = \iint_S n_j p_{ij}(\mathbf{y}, \tau) \frac{\partial G}{\partial y_i}\, \mathrm{d}^2\mathbf{y}\, \mathrm{d}\tau + \iint_V T_{ij}(\mathbf{y}, \tau) \frac{\partial^2 G}{\partial y_i \partial y_j}\, \mathrm{d}^3\mathbf{y}\, \mathrm{d}\tau \tag{1}$$

where p_a is the acoustic pressure at observer location $\mathbf{x}$ and observer time t, $p_{ij} = p\delta_{ij} - \tau_{ij}$ is the compressive stress tensor composed of pressure p and viscous stress tensor τ_{ij}, n_j is the outward unit normal of the rough-wall surface S, G is an acoustic Green's function, and T_{ij} is the Lighthill stress tensor dominated by the unsteady Reynolds stress $\rho u_i u_j$. Both p_{ij} and T_{ij} are functions of source location $\mathbf{y}$ and source time τ.

Equation (1) is formally exact regardless of the choice of Green's function. For an acoustically compact roughness element on a large rigid flat surface, it is most convenient to employ the half-space Green's function

$$G = \frac{\delta(t - \tau - r/c_0)}{4\pi r} + \frac{\delta(t - \tau - r^*/c_0)}{4\pi r^*} \tag{2}$$

where $r = |\mathbf{x} - \mathbf{y}|$ is the distance between source and observer, $\mathbf{x}^* = (x_1, -x_2, x_3)$ is the image of observer position $\mathbf{x}$ in the wall, and $r^* = |\mathbf{x}^* - \mathbf{y}|$. The normal derivative $\partial G/\partial n$ vanishes on the flat surface $y_2 = 0$ but not on the surface of the roughness element. Substituting Eq. (2) into Eq. (1) leads to

$$\begin{aligned} p_a(\mathbf{x}, t) = &-\frac{\partial}{\partial x_i} \int_{S_r} \frac{n_j p_{ij}(\mathbf{y}, t - r/c_0)}{4\pi r}\, \mathrm{d}^2\mathbf{y} \\ &- \frac{\partial}{\partial x_i^*} \int_{S_r} \frac{n_j p_{ij}(\mathbf{y}, t - r^*/c_0)}{4\pi r^*}\, \mathrm{d}^2\mathbf{y} \\ &+ \frac{\partial}{\partial x_\alpha} \int_{S-S_r} \frac{\tau_{\alpha 2}(\mathbf{y}, t - r/c_0)}{2\pi r}\, \mathrm{d}^2\mathbf{y} \\ &+ \frac{\partial^2}{\partial x_i \partial x_j} \int_V \frac{T_{ij}(\mathbf{y}, t - r/c_0)}{4\pi r}\, \mathrm{d}^3\mathbf{y} \\ &+ \frac{\partial^2}{\partial x_i^* \partial x_j^*} \int_V \frac{T_{ij}(\mathbf{y}, t - r^*/c_0)}{4\pi r^*}\, \mathrm{d}^3\mathbf{y} \end{aligned} \tag{3}$$

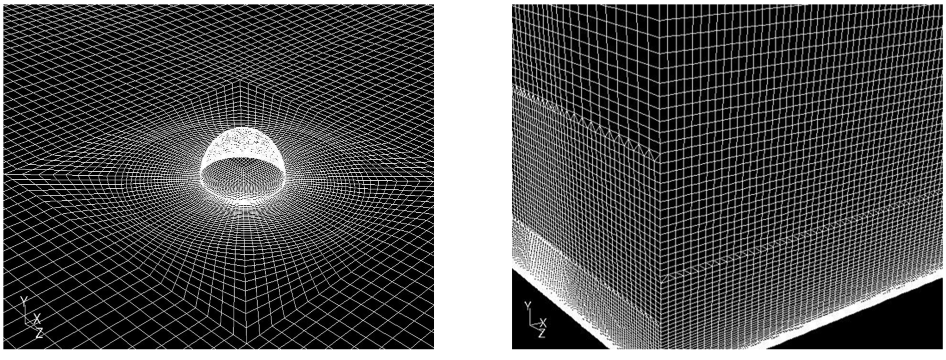

a) b)

Fig. 2 Computational mesh for a single hemispherical roughness element on a plane wall: a) surface mesh near the hemisphere, and b) boundary-layer mesh near inlet. Only 1 in 2 mesh lines in each direction is plotted for clarity.

where S_r denotes the surface of the roughness element, and $S - S_r$ is the flat surface. On a smooth surface, S_r is absent, and Eq. (3) reduces to Powell's result [1] (see also [15]). When a roughness element is present, however, the first two terms dominate sound radiation for flows at low Mach numbers and high Reynolds numbers because of their dipole nature. The third term, which represents the dipole sound generated by unsteady viscous shear stress on the flat surface, is generally negligible except at low Reynolds numbers. The last two terms represent contributions from distributed volume quadrupoles and their images in the wall, which are $O(M)$ (M being the freestream Mach number) smaller than dipole sound. Approximating Eq. (3) by the first two terms and taking the acoustic far-field limit ($r \gg \lambda$), it can be shown that

$$p_a(\mathbf{x},t)=\frac{1}{4\pi c_0}\frac{\partial}{\partial t}\int_{S_r}\left[\frac{r_i}{r^2}n_j p_{ij}\left(\mathbf{y},t-\frac{r}{c_0}\right)+\frac{r_i^*}{r^{*2}}n_j p_{ij}\left(\mathbf{y},t-\frac{r^*}{c_0}\right)\right]\mathrm{d}^2\mathbf{y} \qquad (4)$$

This is simply the surface-integral part of Curle's equation [10], accounting for the image of the roughness element in the wall.

If the roughness element is acoustically compact, $D \ll \lambda$, then $r \approx r^* \approx |\mathbf{x}-\mathbf{y}_c| \equiv R$, where $\mathbf{y}_c$ is the central position of the base of the roughness element on the plane $y_2 = 0$. Equation (4) can be further simplified to

$$p_a(\mathbf{x},t)=\frac{R_\alpha}{2\pi c_0 R^2}D_\alpha\left(t-\frac{R}{c_0}\right) \qquad (5)$$

where

$$D_i(t)=\frac{\mathrm{d}}{\mathrm{d}t}\int_{S_r} n_j p_{ij}(\mathbf{y},t)\,\mathrm{d}^2\mathbf{y} \qquad (6)$$

Note that the dipole source function D_α is the time derivative of the net unsteady force exerted on the fluid by the surface of the roughness element. The repeated index α implies summation over 1 and 3, which suggests that only the net force in the streamwise and spanwise directions contributes to dipole sound radiation. The wall-normal components in Eq. (4) do not survive a multipole expansion to the leading order and are therefore relegated to acoustic quadrupoles. A physical explanation is that the strength of dipoles in the streamwise and spanwise directions is doubled due to constructive interference with their images in the wall, whereas the lift dipole in the wall-normal direction interferes destructively with its image to form a less efficient quadrupole source. All quadrupole terms are neglected in the present calculation. If better accuracy is required, one can add quadrupole corrections to the surface integral and the volume quadrupole terms in Eq. (3). Once the dipole source functions D_α are obtained from the flowfield simulation discussed earlier, the leading-order acoustic pressure $p_a(\mathbf{x},t)$ can be calculated anywhere in the far field.

If there are N roughness elements based at $\mathbf{y}_c^{(n)}$ on the flat surface and $R^{(n)} = |\mathbf{x}-\mathbf{y}_c^{(n)}|$, the total far-field acoustic pressure is simply the sum of their individual contributions:

$$p_a(\mathbf{x},t)=\frac{1}{2\pi c_0}\sum_{n=1}^{N}\frac{R_\alpha^{(n)}}{R^{(n)2}}D_\alpha^{(n)}\left(t-\frac{R^{(n)}}{c_0}\right) \qquad (7)$$

where the superscript (n) indicates the quantity for the nth roughness element, and

$$D_i^{(n)}(t)=\frac{\mathrm{d}}{\mathrm{d}t}\int_{S_r^{(n)}} n_j p_{ij}(\mathbf{y},t)\,\mathrm{d}^2\mathbf{y} \qquad (8)$$

It should be noted that the formulation presented here does not account for the effect of sound-flow interaction. This is a valid approximation for long wavelengths relative to the boundary-layer thickness. This formulation is invalid for short wavelengths or propagation at grazing angles, at which refraction and scattering of acoustic waves by the nonuniform and turbulent velocity field along their paths become important.

III. Results and Discussion

A. Flowfield and Validation

An instantaneous flowfield in terms of the streamwise velocity in a spanwise cut through the center of the hemisphere is depicted in Fig. 3. Figure 3a provides a global view of the large disparity of flow scales captured by the LES, ranging from the very fine near-wall structures to large eddies that scale with the boundary-layer thickness. It also illustrates the smallness of the hemisphere, based at $x = y = 0$, relative to the boundary-layer thickness. A close-up view near the hemisphere is given in Fig. 3b. It shows two unsteady recirculation regions, one upstream and the other downstream of the hemisphere (as will be discussed further in Sec. III.C). The small recirculation zone in front of the hemisphere is evidence of a horseshoe-vortex system generated by the strong adverse pressure

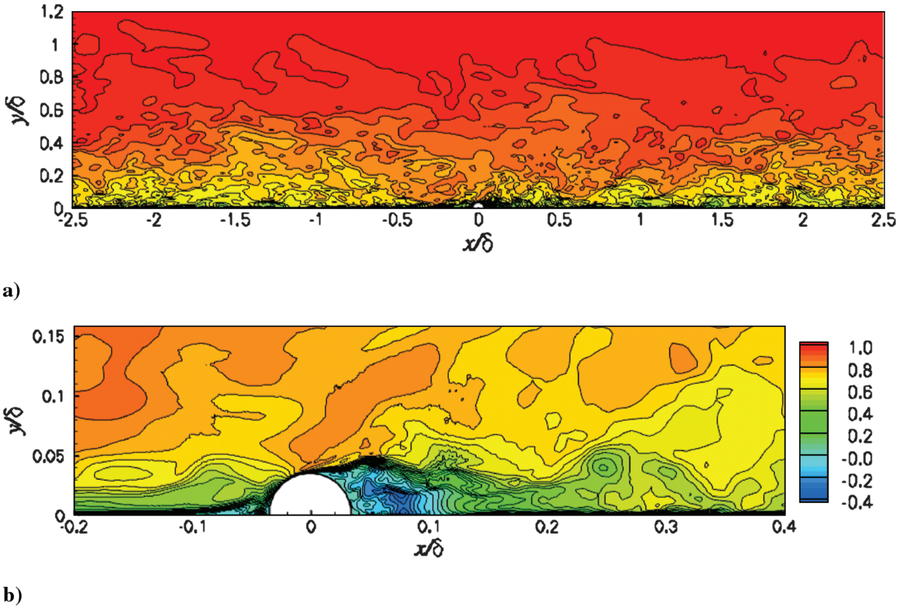

Fig. 3 Isocontours of instantaneous streamwise velocity u/U_∞ in the plane $z = 0$: a) global view, and b) close-up view near the hemisphere. Twenty-nine evenly distributed levels from −0.4 to 1 are plotted.

gradient upstream of the hemisphere, as was also observed experimentally by Bennington [26]. Similar observations were made by George and Simpson [29] in the case of a cylindrical roughness element. The large recirculation zone behind the hemisphere is generated by the separated shear layer and its breakdown due to Kelvin–Helmholtz instability.

Figure 4 provides another perspective of the turbulent flow around the hemisphere through contours of vorticity magnitude ω in the plane $y = h/2$ at a time instant. It clearly shows breakdown of the shear layer in the wake and distortion of the near-wall elongated streaky structures as they approach the hemisphere from upstream. A three-dimensional view of the flow is provided in Fig. 5, which depicts the second invariant of the velocity gradient [30] at two contour levels. This quantity, defined as $Q = -(S_{ij}S_{ji} + \Omega_{ij}\Omega_{ji})/2$, where $S_{ij} = (\partial u_i/\partial x_j + \partial u_j/\partial x_i)/2$ and $\Omega_{ij} = (\partial u_i/\partial x_j - \partial u_j/\partial x_i)/2$, is widely used to visualize coherent vortical structures in a turbulent flowfield. The isosurfaces in this figure show that horseshoe-vortex structures are formed around the junction between the hemisphere and plane wall and, as the incoming flow impinges on the hemisphere, a thin shear layer is formed. There are strong interactions among the newly generated structures and also between these structures and incoming turbulence. Downstream of the hemisphere, the shear layer breaks down shortly after it separates from the hemispheric surface, creating an intensive turbulent region in the wake. Note that, in both Figs. 4 and 5, no large-scale von-Kármán-type vortex street is observed and the wake is confined to a relatively small region downstream of the hemisphere featuring shear-layer instability and small-scale vortex shedding. The local Reynolds number based on roughness height and mean approaching velocity at the roughness height calculated from the simulation is approximately 1740.

A quantitative validation of the LES flowfield is shown in Figs. 6 and 7 in comparison with the LDV measurements of Bennington [26]. In Fig. 6 profiles of velocity statistics along the y direction are plotted at a location $1.36D$ downstream of the center of the hemisphere. They are, from left to right, the mean streamwise velocity, mean wall-normal velocity, and the streamwise, wall-normal, and spanwise components of Reynolds normal stress. The

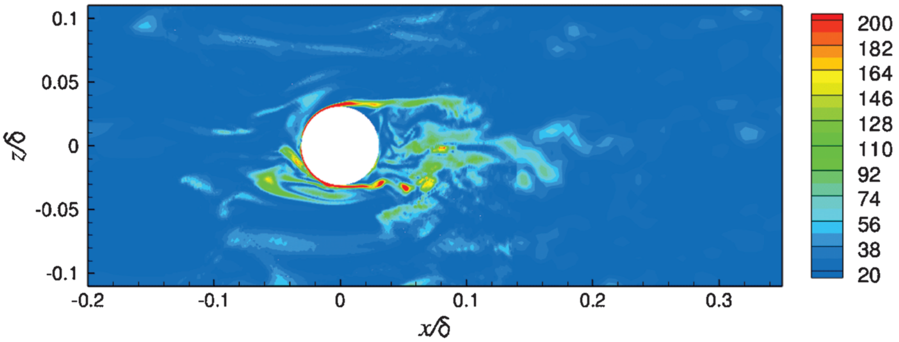

Fig. 4 **Isocontours of instantaneous vorticity magnitude $\omega\delta/U_\infty$ in plane $y = h/2$. Nineteen evenly distributed levels from 20 to 200 are plotted.**

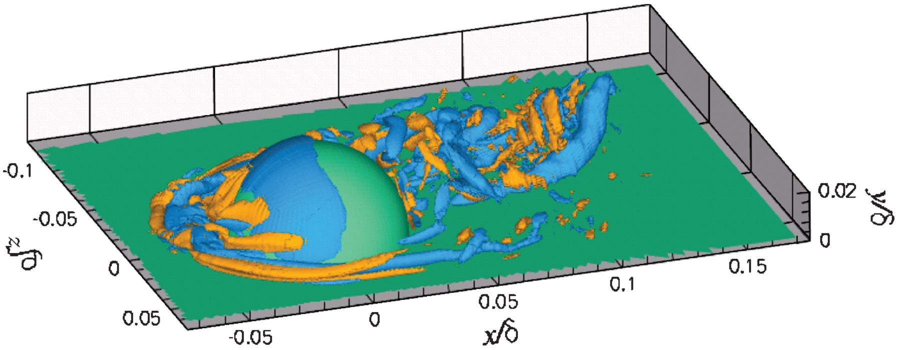

Fig. 5 **Isosurfaces of the second invariant of velocity gradient $Q(\delta/U_\infty)^2$ at a time instant. Two values at ±1000 are plotted.**

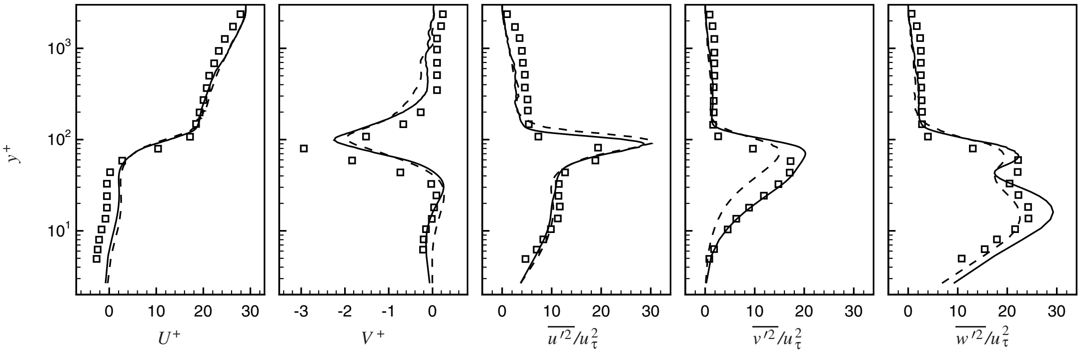

Fig. 6 **Profiles of velocity statistics along y direction at location $x = 1.36D$, $z = 0$. Squares: experiment [26], solid line: LES, dashed line: LES with coarse mesh.**

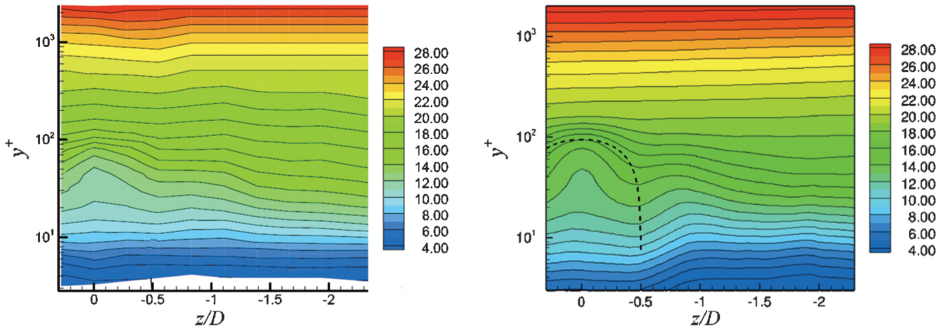

a) U^+

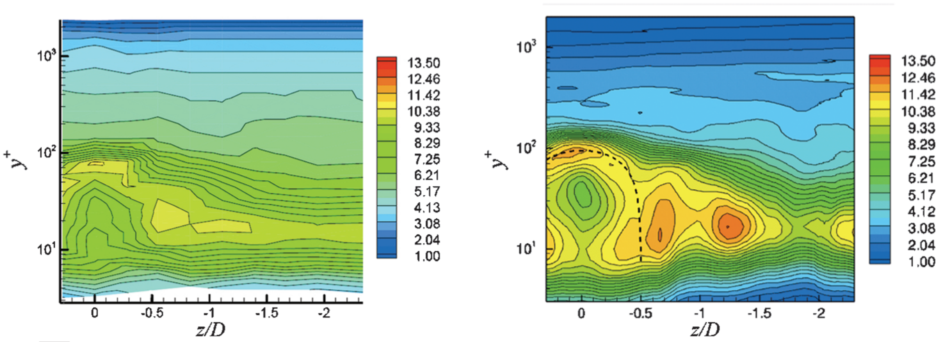

b) $\overline{u'^2}/u_\tau^2$

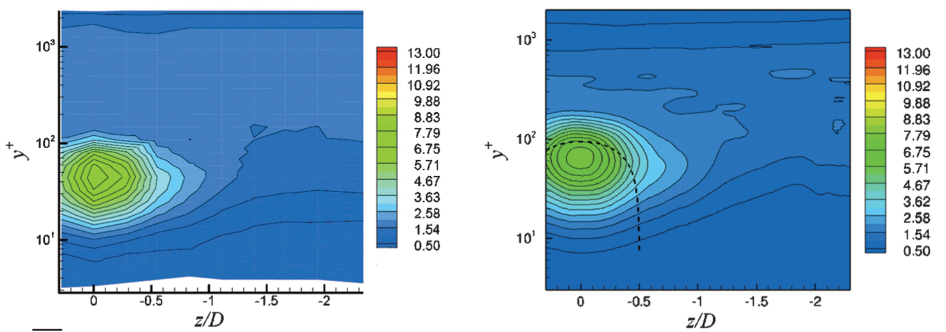

c) $\overline{v'^2}/u_\tau^2$

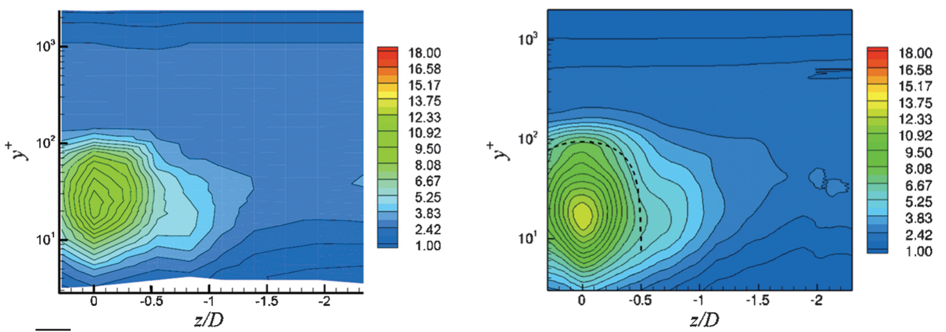

d) $\overline{w'^2}/u_\tau^2$

Fig. 7 Isocontours of velocity statistics in the plane $x = 2.75D$. Left: experiment [26], right: LES. Dashed curves represent outlines of the hemisphere.

agreement between the LES (solid lines) and experiment [26] (symbols) is reasonable. The length of the mean recirculation zone is underpredicted, as suggested by the smaller mean streamwise velocity deficit in Fig. 6. The wake velocity fluctuations are somewhat overpredicted, particularly for the streamwise component.

To test the effect of grid resolution, a coarse-mesh simulation on a grid with only one-half of the original resolution in each direction was performed. The results are shown in Fig. 6 as dashed lines. Considering the drastically reduced grid resolution, which renders the near-wall resolution quite poor, the comparison with the fine-mesh results is acceptable.

Figure 7 shows a comparison of contours of the mean streamwise velocity and three Reynolds normal stress components in a y–z plane further downstream at $x/D = 2.75$. The outline of the hemisphere is represented by the dashed curves in the LES plots (note the distortion due to the linear-log coordinates used). The overall agreement between the numerical (right) and experimental (left) results is again reasonable. The size of the wake region appears to be slightly overpredicted. The largest discrepancy occurs in $\overline{u'^2}$, which is overpredicted by LES by a maximum of approximately 15%.

The overall uncertainties in the LDV measurements are reported [26] to be ±0.28 for U^+, ±0.7 for V^+, ±0.51 for $\overline{u'^2}/u_\tau^2$, ±0.06 for

$\overline{v'^2}/u_\tau^2$, and ±0.11 for $\overline{w'^2}/u_\tau^2$. The converged velocity statistics from LES are obtained by averaging over a time period of approximately $80\delta/U_\infty$, or 16 flow-through times based on a streamwise domain length of 5δ.

B. Sound from a Single Roughness Element

The dimensionless acoustic dipole source functions evaluated using Eq. (6) with LES data are shown in Fig. 8 for 10 dimensionless time units. Interestingly, the spanwise drag dipole (Fig. 8b) exhibits a larger magnitude than that of the streamwise dipole (Fig. 8a). It is also noted that the pressure contribution to the drag dipoles (solid lines) is more than an order of magnitude larger than the contribution from viscous stress (dashed lines). This suggests that sound generation is drastically enhanced by surface roughness primarily due to unsteady form drag. In a smooth-wall turbulent boundary layer, the drag dipoles arise from unsteady viscous wall stress only [1–4] and are therefore relatively weak. Hu et al. [4] showed that in this case the sound intensity due to viscous wall stress is more than 10 dB higher in the streamwise direction than in the spanwise direction.

The acoustic directivity in the far field is shown in Fig. 9 in two perpendicular planes, $x = 0$ and $z = 0$, both cutting through the center of the hemisphere. The directivity is measured in terms of the mean square of the acoustic pressure $\overline{p_a^2}/M^2(\rho U_\infty^2)^2$ at a distance $r/\delta = 100$ from the center of the hemisphere. It confirms that the spanwise dipole radiation, shown in the $x = 0$ plane, is stronger than the streamwise dipole radiation shown in the $z = 0$ plane. The difference is approximately 2.4 dB in their peak values.

Sound pressure spectra at three far-field locations, $\mathbf{x}/\delta = (50, 50, 0)$, (0, 50, 50), and $(50/\sqrt{2}, 50, 50/\sqrt{2})$, are plotted in Fig. 10. These three locations are of the same distance, $r/\delta = 50\sqrt{2}$, from the center of the hemisphere. The first and second positions receive sound signals only from the streamwise dipole and spanwise dipole, respectively; therefore, their spectra are representative of the streamwise and spanwise dipole radiation. The third position receives signals from both dipoles. It is observed from Fig. 10 that the stronger spanwise dipole radiation lies in the lower frequency range of $f\delta/U_\infty < 5$, with a broadband peak around frequency $f_{\max}\delta/U_\infty \approx 1.7$. In contrast, the streamwise dipole sound spectrum is relatively flat at low frequencies.

The sound directivity and spectra in Figs. 9 and 10 are calculated using source data collected over a time period of $67\delta/U_\infty$, or 13.4 flow-through times, with a sampling resolution of $8.4 \times 10^{-4}\delta/U_\infty$. Both quantities are converged statistically.

It is instructive to interpret the results in Fig. 10 in dimensional terms under the experimental conditions mentioned earlier. The peak frequency corresponds to $f_{\max} = 1199$ Hz based on $\delta = 39$ mm and $U_\infty = 27.5$ m/s. At this frequency, the sound spectral level at $\mathbf{x} = (0, 2, 2)$ m is approximately −11 dB/Hz, or 2 dB if integrated over a 20 Hz bin width, with reference to 2×10^{-5} Pa. Although the sound level from such a single roughness element is low, it becomes significant when a large number of distributed roughness elements are present. For example, with 1000 sparsely distributed (hence, no interaction) roughness elements, the peak spectral level becomes 32 dB per 20 Hz bin width. In addition, in the nonsparse case, interaction with wakes from upstream roughness elements can

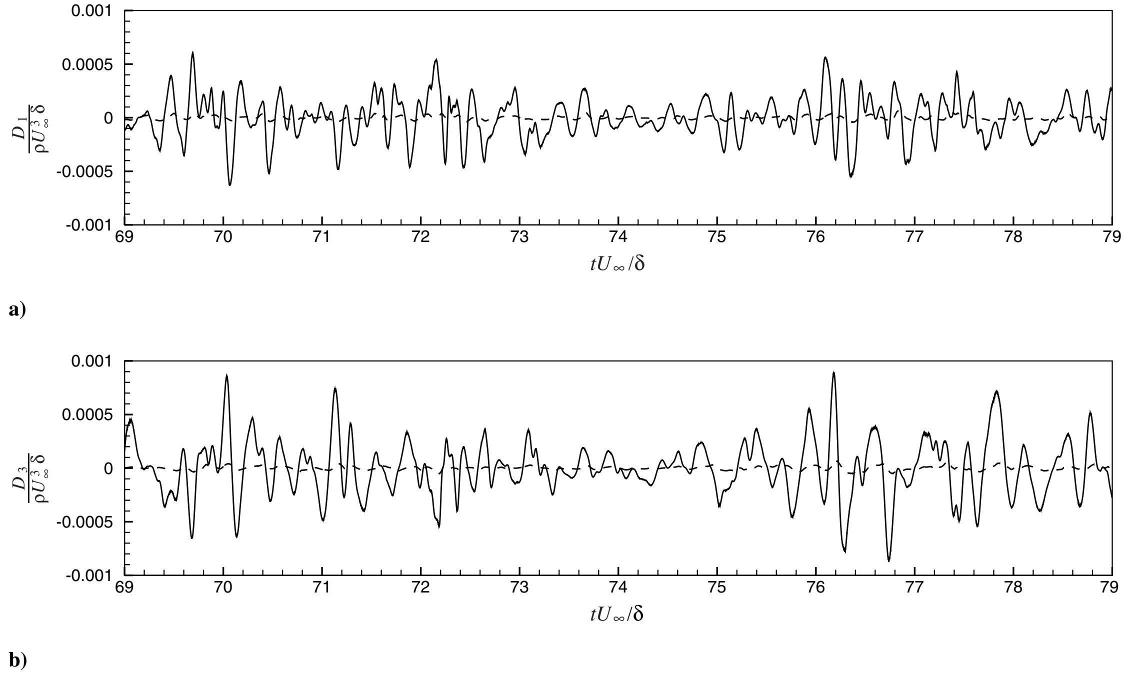

Fig. 8 Time series of dipole source functions: a) streamwise component $D_1/(\rho U_\infty^3 \delta)$, and b) spanwise component $D_3/(\rho U_\infty^3 \delta)$. Solid line: contribution from unsteady pressure p, dashed line: contribution from viscous stress τ_{ij}.

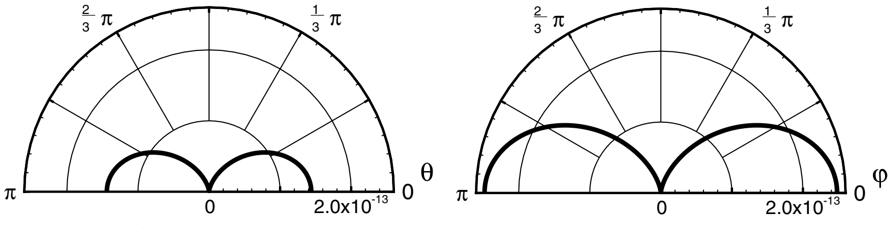

a) In plane $z = 0$

b) In plane $x = 0$

Fig. 9 Far-field directivity in terms of $\overline{p_a^2}/(M^2(\rho U_\infty^2)^2)$ at a distance of $r/\delta = 100$ from the center of the hemisphere: a) spanwise plane $z = 0$, and b) streamwise plane $x = 0$.

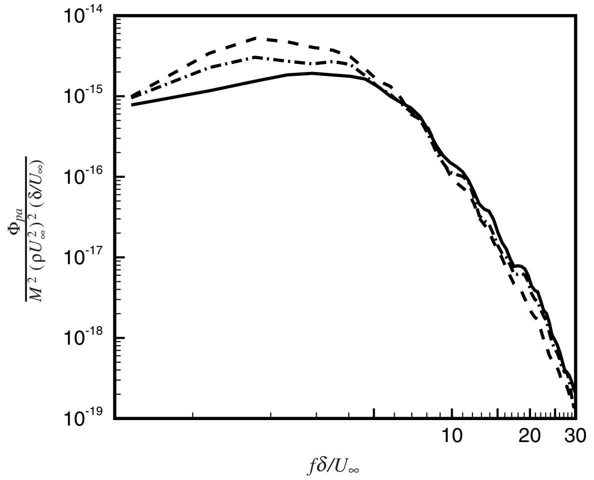

Fig. 10 Acoustic pressure spectra at three far-field locations of equal distances from the hemisphere. Solid line: $x/\delta = (50, 50, 0)$, dashed line: $x/\delta = (0, 50, 50)$, chain-dot line: $x/\delta = (50/\sqrt{2}, 50, 50/\sqrt{2})$.

significantly enhance the roughness noise, as will be illustrated in Sec. III.D.

C. Source Mechanisms

An understanding of source mechanisms for roughness noise is not only of fundamental interest but also critically important for developing predictive models. Diffraction of incident hydrodynamic pressure fluctuations in a turbulent boundary layer by roughness elements [5] plays a dominant role if the roughness elements do not penetrate beyond the buffer layer. In the present study, the roughness height $h^+ = 95$, which is deep in the logarithmic layer. Turbulence distortion and generation associated with bluff-body junction flow [9] are expected to be very important to sound generation. As discussed in Sec. II.B, the dipole sound radiation is related to hemispheric surface-pressure fluctuations through Eqs. (5) and (6). Hence, source mechanisms can be analyzed by examining the underlying causes for surface-pressure fluctuations. As turbulent eddies from upstream impinge on the hemisphere, turbulent kinetic energy is converted to surface-pressure fluctuations. In addition, as shown earlier, turbulent horseshoe vortices and the shear-layer breakdown in the wake are also potential sources of pressure fluctuations on the surface of the hemisphere. Because these mechanisms act on different parts of the hemispheric surface, their relative importance can be assessed by examining the distribution of wall-pressure fluctuations and their frequency spectra. As with the sound pressure spectra, the surface-pressure statistics presented in this section are collected over a time period of $67\delta/U_\infty$, or 13.4 flow-through times, with a sampling resolution of $8.4 \times 10^{-4}\delta/U_\infty$.

Figure 11a shows the rms of the pressure fluctuations, $p'_{\rm rms}(x, z)$, on the hemispheric surface and the surrounding wall as viewed from above. In this figure, the highest pressure-fluctuation intensity is observed around the front edge of the hemisphere, which is closest to the heads of the horseshoe vortices, as shown in Fig. 5. Higher levels of pressure fluctuations occur on the front half of the hemisphere, upon which the incoming turbulent eddies impinge, than the back half. Pressure fluctuations on the back half of the hemisphere are relatively weak because of shear-layer separation, which creates a low-speed recirculation zone above the surface (cf. Figs. 3 and 4). The breakdown of the shear layer and unsteady flow reattachment on the flat wall generate strong unsteady wall pressure a short distance downstream of the hemisphere, where two local peaks symmetric about $z = 0$ are observed.

To determine important regions contributing to the streamwise and spanwise dipoles specifically, the rms values of the integrand in Eq. (6) are evaluated. Figures 11b and 11c show rms values of $n_x p'$ and $n_z p'$, which represent the unsteady drag forces per unit surface area in the streamwise and spanwise directions, respectively. Only pressure contributions are considered because viscous contributions

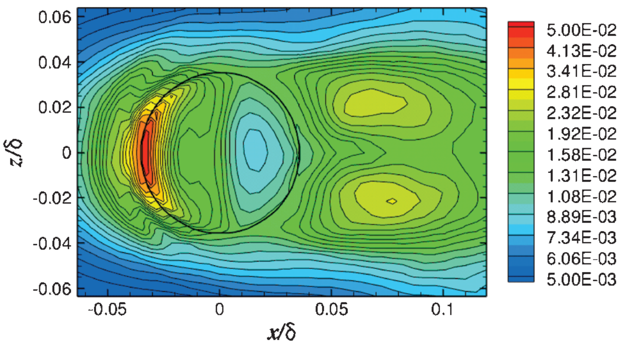

a) $p'_{rms}(x, z)\,/\,(\rho U_\infty^2)$

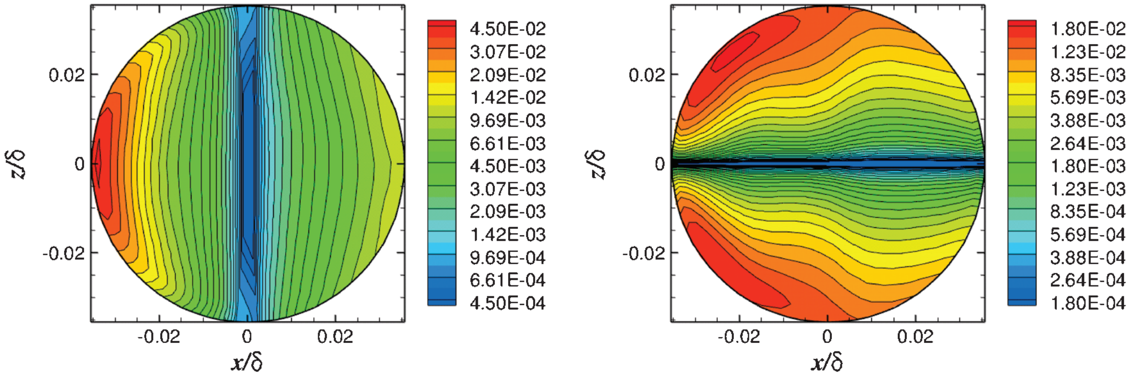

b) $|n_x|\,p'_{rms}(x, z)\,/\,(\rho U_\infty^2)$ **c)** $|n_z|\,p'_{rms}(x, z)\,/\,(\rho U_\infty^2)$

Fig. 11 Top views of isocontours of rms of wall-pressure fluctuations and its decomposition in the streamwise and spanwise directions. Twenty-five logarithmically distributed levels are plotted. Circles represent borders of the hemisphere.

are negligible, as shown in Fig. 8. It is found that the nose region of the hemisphere contributes most to the streamwise unsteady drag and, hence, the streamwise dipole. The contribution decays rapidly with x and becomes identically zero at $x = 0$, where $n_x = 0$. The contribution from the back half of the hemisphere to the streamwise dipole is relatively small. For the spanwise unsteady drag and dipole radiation, the important regions are around the hemispheric edge at approximately ±45 deg from upstream, suggesting the legs of horseshoe vortices and incoming turbulent eddies as major physical sources.

The important source regions for different frequencies can be identified by examining the power spectral density of the wall-pressure fluctuations, $\Phi_{pp}(f, x, z)$. Figures 12 and 13 show Φ_{pp} and its contributions to the dipole sources at two different frequencies of $f\delta/U_\infty = 1.7$ and 13.6, respectively. The first frequency corresponds to the broad peak of spanwise dipole radiation, whereas the second frequency is representative of the high-frequency range in the acoustic spectra in Fig. 10. The quantities $|n_x|^2\Phi_{pp}$ and $|n_z|^2\Phi_{pp}$ are indicative of contributions to the streamwise and spanwise acoustic radiative power in frequency space. A comparison of these two figures shows that, at low frequencies, the important region for sound radiation is closer to the leading edge of the hemisphere, particularly for the spanwise dipole radiation. At higher frequencies, the wake area shows greater pressure fluctuations than at lower frequencies. The relative contributions from the back half of the hemisphere to both the streamwise and spanwise dipole radiation are increased, although they are still not as strong as those from the front half.

Figures 14 and 15 are plotted to demonstrate the relationship between wall-pressure fluctuations and the hydrodynamic flowfield. Figure 14 shows the instantaneous two-dimensional streamlines together with contours of instantaneous pressure, and Fig. 15 shows the time-averaged streamlines with contours of rms values of pressure fluctuations, both in the central spanwise plane $z = 0$. The steep adverse pressure gradient in front of the hemisphere gives rise to a major horseshoe vortex and a secondary one as indicated by the mean streamlines. The low-pressure core of the horseshoe vortex is clearly visible in Fig. 14. Figure 15 shows strong pressure fluctuations at the mean vortex-core location due to unsteady motions of the vortex. The stagnation point on the front surface of the hemisphere corresponds to the highest level of pressure fluctuations, which is more than an order of magnitude larger than that in the turbulent boundary layer unaffected by the hemisphere. Note that the stagnation point is lifted from the bottom corner due to the presence of the horseshoe vortices. Clearly, the horseshoe vortices play an important role in amplifying the pressure fluctuations in the front region of the hemispheric surface. In the wake of the hemisphere, shear-layer breakdown causes strong pressure fluctuations, but these pressure fluctuations are off the surface of the hemisphere and, thus, do not contribute to acoustic dipoles. The back half of the hemisphere is in a low-speed recirculation zone with weak unsteady pressure and, therefore, has a much smaller impact on the dipole sound radiation.

From these observations, it can be concluded that incoming turbulent eddies impinging on the front half of the hemisphere play a dominant role in both streamwise and spanwise dipole sound radiation. The horseshoe vortices, interacting with incoming turbulence and the hemisphere, further amplify the dipole sound. The shear-layer breakdown and resulting unsteady wake, once regarded as major sources of self-noise, are found to be relatively unimportant in this single-hemisphere case. The contribution from the unsteady wake rises with increasing frequency for both streamwise and spanwise dipole radiation, but it remains small compared with contributions from incident turbulence and horseshoe vortices.

D. Wake Effect

Real rough surfaces contain a large number of roughness elements. It is therefore important to understand the interaction of a roughness element with the wakes of upstream roughness elements and its impact on sound generation. To this end, a simulation is performed with a pair of hemispherical roughness elements of the

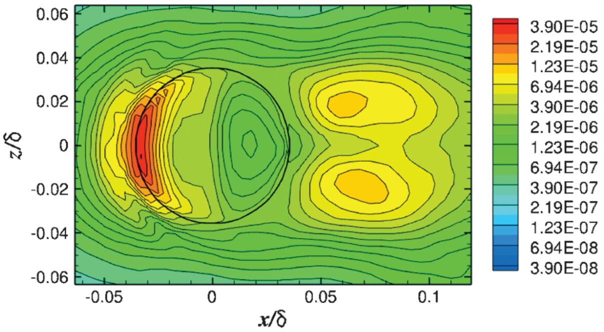

a) $\dfrac{\Phi_{pp}(f, x, z)}{(\rho U_\infty^2)^2 \;\; (\delta/U_\infty)}$

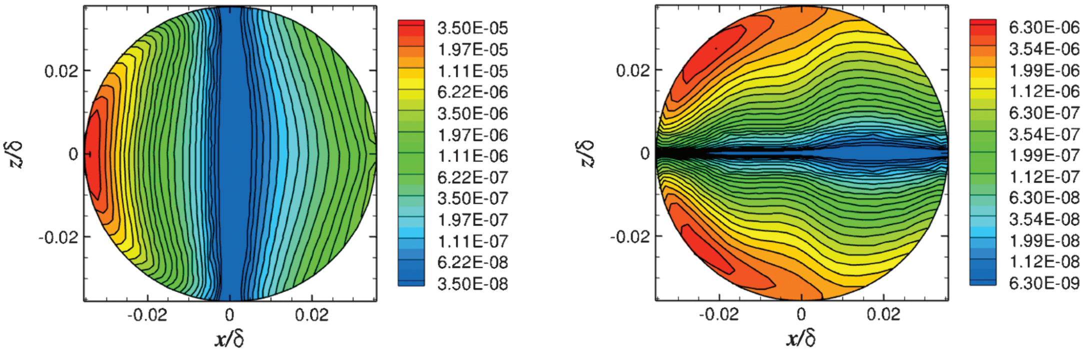

b) $|n_x|^2 \dfrac{\Phi_{pp}(f, x, z)}{(\rho U_\infty^2)^2 \;\; (\delta/U_\infty)}$

c) $|n_z|^2 \dfrac{\Phi_{pp}(f, x, z)}{(\rho U_\infty^2)^2 \;\; (\delta/U_\infty)}$

Fig. 12 Top views of isocontours of power spectral density of wall-pressure fluctuations and its decomposition in streamwise and spanwise directions at frequency $f\delta/U_\infty = 1.7$. Twenty-five logarithmically distributed levels are plotted. Circles represent borders of the hemisphere.

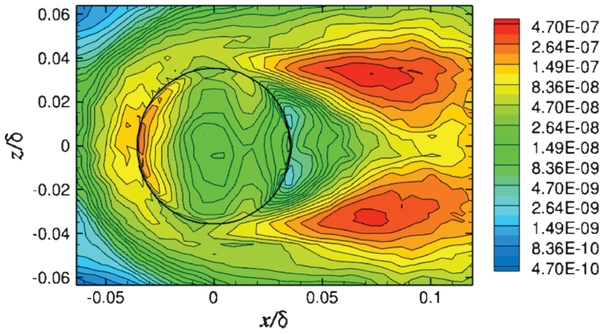

a) $\frac{\Phi_{pp}(f, x, z)}{(\rho U_\infty^2)^2\ (\delta/U_\infty)}$

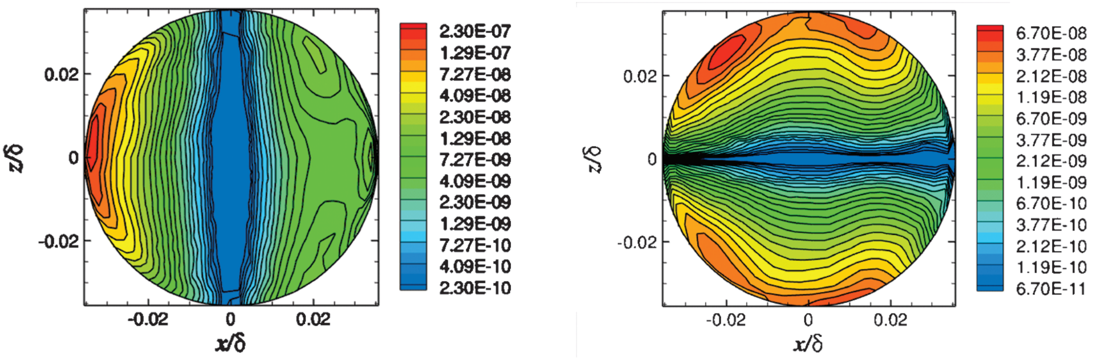

b) $|n_x|^2 \frac{\Phi_{pp}(f, x, z)}{(\rho U_\infty^2)^2\ (\delta/U_\infty)}$

c) $|n_z|^2 \frac{\Phi_{pp}(f, x, z)}{(\rho U_\infty^2)^2\ (\delta/U_\infty)}$

Fig. 13 Top views of isocontours of power spectral density of wall-pressure fluctuations and its decomposition in streamwise and spanwise directions at frequency $f\delta/U_\infty = 13.6$. Twenty-five logarithmically distributed levels are plotted. Circles represent borders of the hemisphere.

same size as the single hemisphere considered earlier. The two hemispheres are aligned in the streamwise direction and separated by a distance of $5.5h$ between their centers, with the downstream hemisphere based at the center of the plane wall ($\mathbf{y}_c = (0, 0, 0)$). This configuration places the downstream hemisphere under the strong influence of the wake of the upstream one.

An instantaneous flowfield from this simulation is shown in Figs. 16a and 16b, which depict contours of vorticity magnitude in the planes $z = 0$ and $y = h/2$, respectively. The turbulence structures impinging on the downstream hemisphere are generated primarily by the upstream hemisphere and are much more energetic than those in the unperturbed boundary layer. New vortical structures formed around the base of the downstream hemisphere resemble the horseshoe vortices observed around the upstream one or a single hemisphere, but they are less coherent, particularly in the nose region. The shear layer from the downstream hemisphere breaks down shortly

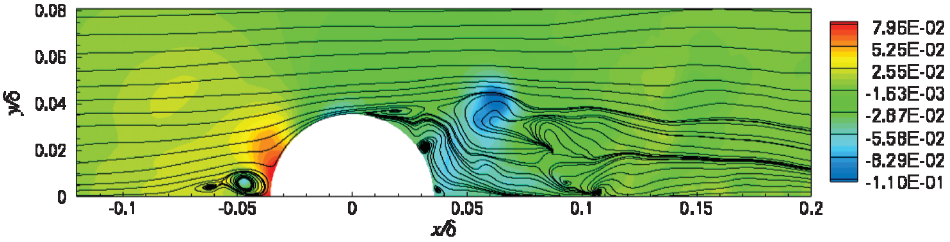

Fig. 14 Instantaneous streamlines and isocontours of instantaneous pressure $p/(\rho U_\infty^2)$ in the plane $z = 0$. Twenty-nine evenly distributed contour levels for pressure are plotted.

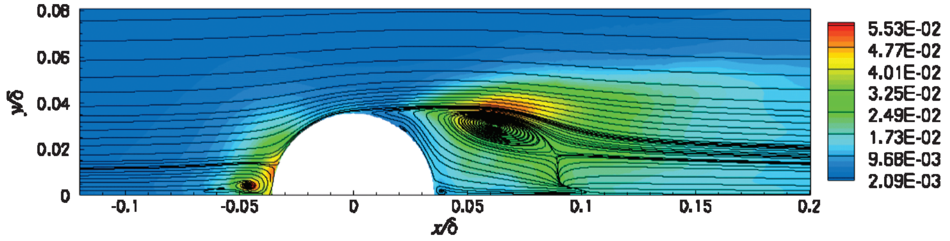

Fig. 15 Time-averaged streamlines and isocontours of rms of pressure fluctuations $p'_{\mathrm{rms}}/(\rho U_\infty^2)$ in the plane $z = 0$. Twenty-nine evenly distributed contour levels for rms pressure are plotted.

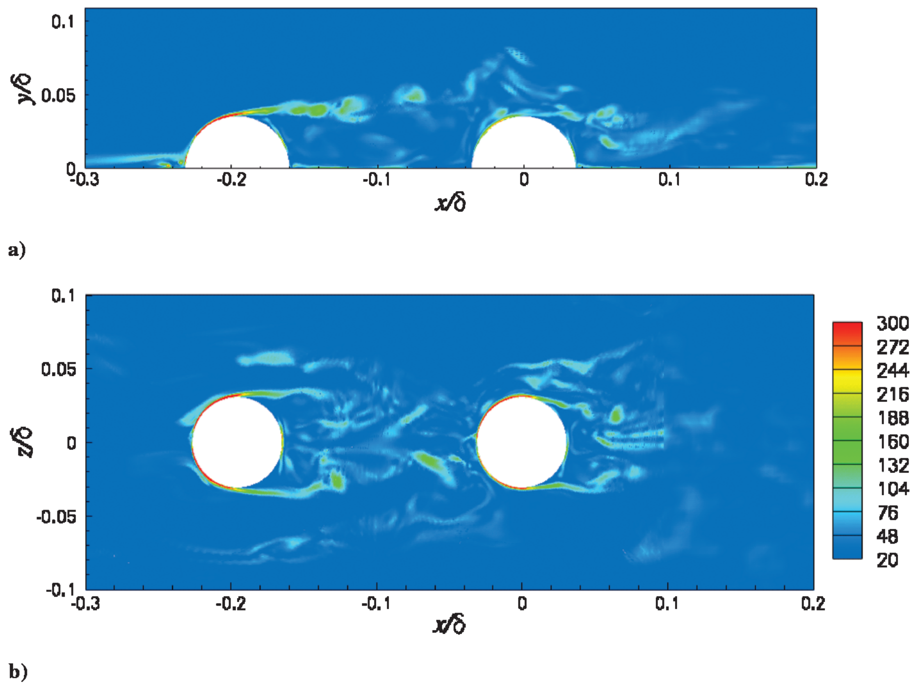

Fig. 16 Isocontours of instantaneous vorticity magnitude $\omega\delta/U_\infty$ for the case with two hemispheres: a) spanwise plane $z = 0$, and b) wall-parallel plane $y = h/2$.

after separation due to the strong perturbation caused by the upstream wake, creating a smaller recirculation bubble compared with the one behind the upstream hemisphere.

As a result of the impinging turbulent wake, stronger pressure fluctuations are found over a larger frontal area of the downstream hemisphere, as shown in Fig. 17, which provides a top view of the rms values of pressure fluctuations on the two hemispheres and the surrounding plane wall. The statistics are averaged over a period of $24\delta/U_\infty$. The distribution of p'_{rms} on the upstream hemisphere is similar to that in the single-hemisphere case (see Fig. 11), although the wake is wider due to blockage by the downstream hemisphere. On the surface of the downstream hemisphere, the p'_{rms} contours exhibit two strong peaks, corresponding to locations upon which the most energetic eddies shed from the upstream hemisphere impinge (see Fig. 16). Relative to the horseshoe vortices for a single hemisphere, the vortical structures generated near the base of the downstream hemisphere play a less significant role in creating pressure fluctuations and, therefore, sound radiation. The earlier shear-layer breakdown increases the level of pressure fluctuations on the back half of the downstream hemisphere, but it remains small relative to that on the front half.

Figures 18a and 18b show acoustic spectra at two locations, $\mathbf{x}/\delta = (50, 50, 0)$ and $(0, 50, 50)$. The first location receives radiation from streamwise dipoles only, and the second location receives radiation predominantly from spanwise dipoles (there is a negligible contribution from the streamwise dipole of the upstream hemisphere). The spectra are calculated with source-field data collected over a time period of approximately $68\delta/U_\infty$, with a sampling resolution of $9.4 \times 10^{-4}\delta/U_\infty$. The solid and dashed lines represent sound generated by the upstream and downstream hemispheres, respectively, and the chain-dot lines represent the sound generated collectively by both hemispheres, calculated from Eq. (7). As can be expected from the aforementioned flowfield and surface-pressure analyses, radiation from both the streamwise and spanwise dipoles is significantly enhanced for the downstream hemisphere due to its interaction with the wake from upstream. The increase is particularly significant at intermediate-to-high frequencies and for the streamwise dipole sound. This is because the turbulent wake from upstream contains more energetic small-scale structures compared with an equilibrium turbulent boundary layer. The streamwise dipole radiation shows a strong spectral peak near $f\delta/U_\infty = 5$, which is found to correspond to the frequency of shear-layer breakdown for the upstream hemisphere. A comparison of the total sound spectra with contributions from the upstream and downstream hemispheres in Fig. 18 shows that the two hemispheres behave as independent sound sources at high frequencies.

From this analysis, it is concluded that, although the wake of a roughness element does not contribute much to the sound generated

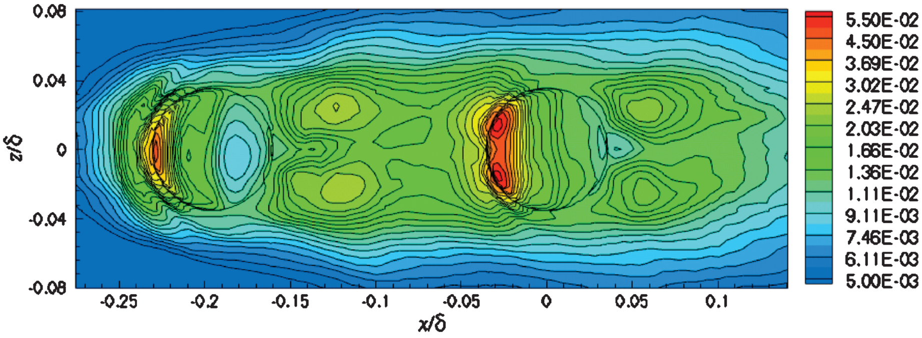

Fig. 17 Top view of isocontours of rms of wall-pressure fluctuations $p'_{\mathrm{rms}}(x, z)/(\rho U_\infty^2)$ for the case with two hemispheres. Twenty-five logarithmically distributed levels are plotted. Circles represent borders of the hemispheres.

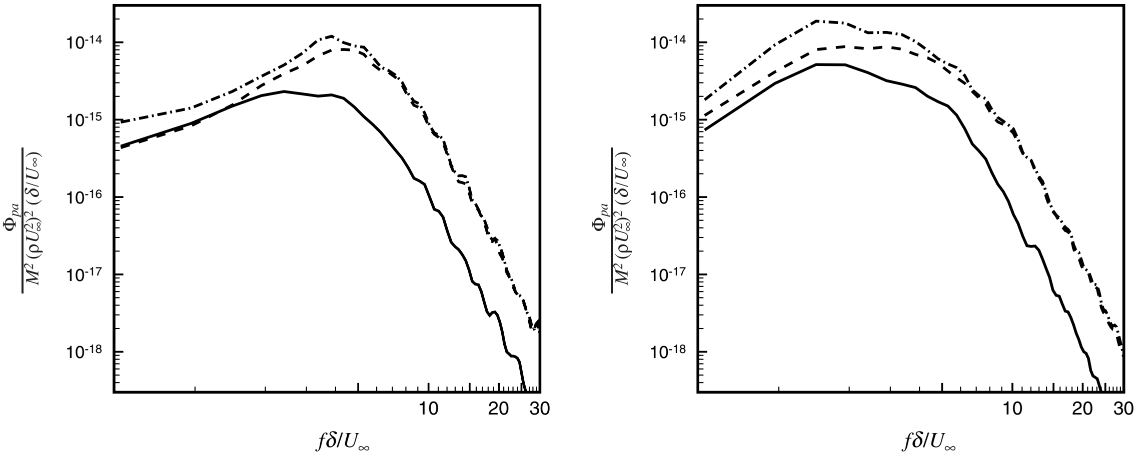

a) x/δ = (50, 50, 0) **b) x/δ = (0, 50, 50)**

Fig. 18 Acoustic pressure spectra at two far-field locations for the case with a pair of hemispheres. Solid line: sound from the upstream hemisphere, dashed line: sound from the downstream hemisphere, chain-dot line: sound from both hemispheres.

by the element itself, it can significantly increase noise radiation from downstream elements through wake-roughness interaction.

IV. Conclusions

In summary, we have performed large-eddy simulations of high-Reynolds-number turbulent boundary-layer flows over a flat plate with a single hemispherical roughness element and a pair of roughness elements. The resulting flowfield statistics for the single-hemisphere case agree with available experimental measurements, demonstrating the feasibility of using LES to study rough-wall boundary-layer noise under experimental flow conditions. The noise calculation based on Lighthill's theory highlighted the importance of unsteady drag, particularly the spanwise component, which has traditionally been overlooked, as the primary noise source. The radiated sound field is stronger in the spanwise direction than in the streamwise direction in the single-element case and of comparable strength in both directions in the double-element case. Pressure fluctuations on the hemisphere and its surrounding wall were investigated to evaluate the relative importance of various source mechanisms. The results suggest that the impingement of incoming turbulence and turbulent horseshoe vortices dominate both streamwise and spanwise dipole radiation over all frequencies. The unsteady wake motions induced by a roughness element, including shear-layer breakdown and vortex shedding, do not contribute significantly to the sound production by the element itself. However, in the presence of a downstream hemisphere, wake-hemisphere interaction significantly enhances sound radiation, particularly in the streamwise direction and at high frequencies.

Acknowledgments

This work was sponsored by the Office of Naval Research (ONR) under grant N00014-06-1-0640, with Ki-Han Kim as program manager. Computer time was provided by the U.S. Department of Defense High Performance Computing Modernization Program through the U.S. Army Research Laboratory Major Shared Resource Center. We wish to thank Minsuk Ji for generating the turbulent inflow data used in the simulations, and Donghyun You, Yaser Khalighi, and Kan Wang for assistance with the LES code and helpful discussions. This work has benefited from stimulating discussions with William K. Blake and other colleagues in ONR's roughness noise program.

References

[1] Powell, A., "Aerodynamic Noise and the Plane Boundary," *Journal of the Acoustical Society of America*, Vol. 32, No. 8, 1960, pp. 982–990. doi:10.1121/1.1908347

[2] Shariff, K., and Wang, M., "A Numerical Experiment to Determine Whether Surface Shear-Stress Fluctuations Are a True Sound Source," *Physics of Fluids*, Vol. 17, 107105, 2005. doi:10.1063/1.2112747

[3] Morfey, C. L., "The Role of Viscosity in Aerodynamic Sound Generation," *International Journal of Aeroacoustics*, Vol. 2, No. 3–4, 2003, pp. 225–240. doi:10.1260/147547203322986124

[4] Hu, Z., Morfey, C. L., and Sandham, N. D., "Sound Radiation from a Turbulent Boundary Layer," *Physics of Fluids*, Vol. 18, 098101, 2006. doi:10.1063/1.2337733

[5] Howe, M. S., "On the Generation of Sound by Turbulent Boundary Layer Flow over a Rough Wall," *Proceedings of the Royal Society of London, Series A: Mathematical and Physical Sciences*, Vol. 395, 1984, pp. 247–263. doi:10.1098/rspa.1984.0100

[6] Howe, M. S., "The Influence of Viscous Surface Stress on the Production of Sound by Turbulent Boundary Layer Flow over a Rough Wall," *Journal of Sound and Vibration*, Vol. 104, No. 1, 1986, pp. 29–39. doi:10.1016/S0022-460X(86)80129-8

[7] Howe, M. S., "Sound Produced by Turbulent Boundary Layer Flow over a Finite Region of Wall Roughness, and over a Forward Facing Step," *Journal of Fluids and Structures*, Vol. 3, 1989, pp. 83–96. doi:10.1016/S0889-9746(89)80013-1

[8] Lighthill, M. J., "On Sound Generated Aerodynamically; I. General Theory," *Proceedings of the Royal Society of London, Series A: Mathematical and Physical Sciences*, Vol. 211, No. 1107, 1952, pp. 564–587. doi:10.1098/rspa.1952.0060

[9] Simpson, R. L., "Junction Flows," *Annual Review of Fluid Mechanics*, Vol. 33, 2001, pp. 415–443. doi:10.1146/annurev.fluid.33.1.415

[10] Curle, N., "The Influence of Solid Boundaries upon Aerodynamic Sound," *Proceedings of the Royal Society of London, Series A: Mathematical and Physical Sciences*, Vol. 231, No. 1187, 1955, pp. 505–514. doi:10.1098/rspa.1955.0191

[11] Smol'yakov, A. V., "Noise of Turbulent Boundary Layer Flow over Smooth and Rough Plates at Low Mach Numbers," *Acoustical Physics*, Vol. 47, No. 2, 2001, pp. 218–225. doi:10.1134/1.1355808

[12] Glegg, S., Devenport, W., and Grissom, D., "Rough Wall Boundary Layer Noise: Theoretical Predictions," AIAA Paper 2007-3417, May 2007.

[13] Smith, B. S., Alexander, W. N., Devenport, W., Glegg, S. A. L., and Grissom, D. L., "The Relationship Between Roughness Noise and the Near-Field Pressure Spectrum," AIAA Paper 2008-2904, May 2008.

[14] Glegg, S., and Devenport, W., "The Far-Field Sound from Rough-Wall Boundary Layers," *Proceedings of the Royal Society of London, Series A: Mathematical and Physical Sciences*, Vol. 465, 2009, pp. 1717–1734. doi:10.1098/rspa.2008.0318

[15] Crighton, D. G., Dowling, A. P., Ffowcs Williams, J. E., Heckl, M., and

Leppington, F. G., *Modern Methods in Analytical Acoustics*, Springer–Verlag, New York, 1991, Chap. 16.

[16] Liu, Y., and Dowling, A. P., "Assessment of the Contribution of Surface Roughness to Airframe Noise," *AIAA Journal*, Vol. 45, No. 4, 2007, pp. 855–869.
doi:10.2514/1.25217

[17] Cole, L. D., "Measurements of Sound Generated by Boundary Layer Turbulence over Smooth and Rough Surfaces," David Taylor Naval Ship Research and Development Center Rept. SAD-288E-1942, Bethesda, MD, July 1980.

[18] Farabee, T. M., and Geib, F. E., Jr., " Measurements of Boundary Layer Pressure Fluctuations at Low Wavenumbers on Smooth and Rough Walls," *Flow Noise Modeling, Measurement, and Control*, NCA-Vol. 11, edited by T. M. Farabee, W. L. Keith, and R. M. Lueptow, American Society of Mechanical Engineers, New York, 1991, pp. 55–68.

[19] Hersh, A. S., "Surface Roughness Generated Flow Noise," AIAA Paper 83-0786, April 1983.

[20] Grissom, D., Devenport, W., and Glegg, S., "Rough Wall Boundary Layer Noise: an Experimental Investigation," AIAA Paper 2007-3418, May 2007.

[21] Anderson, J., Stewart, D., Goody, M., Zoccola, P., and Blake, W., "Sound from Flow Over a Rough Surface," American Society of Mechanical Engineers Paper 2007-41847, Nov. 2007.

[22] Yang, Q., and Wang, M., "Computational Study of Boundary-Layer Noise Due to Surface Roughness," AIAA 2008-2905, May 2008.

[23] Blake, W. K., Kim, K.-H., Goody, M., Wang, M., Devenport, W., and Glegg, S., "Investigations of Roughness-Generated TBL Sound Using Coupled Physical-Computational Experiments in Conjunction with Theoretical Development," *Second ASA-EAA Joint Conference*, Paris, France, July 2008.

[24] Wang, M., Freund, J. B., and Lele, S. K., "Computational Prediction of Flow-Generated Sound," *Annual Review of Fluid Mechanics*, Vol. 38, 2006, pp. 483–512.
doi:10.1146/annurev.fluid.38.050304.092036

[25] Mahesh, K., Constantinescu, G., and Moin, P., "A Numerical Method for Large-Eddy Simulation in Complex Geometries," *Journal of Computational Physics*, Vol. 197, No. 1, 2004, pp. 215–240.
doi:10.1016/j.jcp.2003.11.031

[26] Bennington, J. L., "Effects of Various Shaped Elements in Two-Dimensional High Reynolds Number Turbulent Boundary Layers," M.S. Thesis, Virginia Polytechnic Institute and State Univ., Blacksburg, VA, 2004.

[27] Lund, T. S., Wu, X., and Squires, K., "Generation of Turbulent Inflow Data for Spatially-Developing Boundary Layer Simulations," *Journal of Computational Physics*, Vol. 140, No. 2, 1998, pp. 233–258.
doi:10.1006/jcph.1998.5882

[28] Goldstein, M. E., *Aeroacoustics*, McGraw–Hill, New York, 1976.

[29] George, J., and Simpson, R. L., "Structure of a Two-Dimensional Turbulent Boundary Layer over a Submerged Cylindrical Protuberance," *Proceedings of the Second International Symposium on Turbulence and Shear Flow Phenomena*, Vol. I, pp. 347–352, Stockholm, Sweden, June 2001.

[30] Chong, M. S., Perry, A. E., and Cantwell, B. J., "A General Classification of Three-Dimensional Flow Fields," *Physics of Fluids A*, Vol. 2, No. 5, 1990, pp. 765–777.
doi:10.1063/1.857730

M. Glauser
Associate Editor